VILNIUS TECH
Vilnius Gediminas Technical University

Journal of Civil Engineering and Management
ISSN 1392-3730 / eISSN 1822-3605
2023 Volume 29 Issue 2: 143–156
https://doi.org/10.3846/jcem.2023.18351

STUDY ON FLEXURAL AND DEMOUNTABLE BEHAVIOR OF A MODULAR LIGHT-GAUGE STEEL FRAMED WALL

Cong LIU[1*], Xin CHEN[1], Xiaoyong MAO[1], Lin HE[2], Jian YUAN[3]

[1]*School of Civil Engineering, Suzhou University of Science and Technology, Suzhou, China*
[2]*School of Civil Engineering, Harbin Institute of Technology, Harbin, Heilongjiang, China*
[3]*Rocket Force University of Engineering, Xi'an, China*

Received 24 January 2022; accepted 12 August 2022

Abstract. The demountable and modular light-gauge steel framed (DMLSF) wallboard is presented and used as non-load bearing exterior walls in medium and high-rise steel construction or temporary structure. Firstly, the bending tests were conducted on five wall modules to explore the flexural behavior of the wall. The numerical model was also established and verified by experimental results, and the simplified calculation method of the flexural capacity of the wall was proposed based on 68 numerical models. In addition, the reliability test of the seam between modules was finished to ensure the airtightness of the wall. Furthermore, the demountable behavior of the wall was studied by secondary loading tests and life cycle assessment (LCA) methodology. Results suggested that the wallboard could be used repeatedly after disassembled under the serviceability limit state. Raw materials, especially the insulation material, accounted for a large proportion of the environmental impact of the wallboard. The wallboard's carbon dioxide emission and energy consumption could be significantly reduced when the wallboard was reused. This study can promote the application of the demountable concept in wall components and provide some guidance for the life cycle design of demountable structures.

Keywords: demountable light-gauge steel framed wall, flexural behavior, demountable behavior, environmental impact, life cycle assessment.

Introduction

The construction industry is one of the significant contributors to emissions released and energy consumers. Then the concept of Design for Deconstruction (DfD) of buildings was explored to reduce the energy consumption and material waste related to the construction industry (Parastesh et al., 2014; Xiao et al., 2017; Eckelman et al., 2018). When the needs of the building owners change, the long-term applicability of the building can be realized by disassembling, replacing, recycling, or reusing the structural components. The researches on demountable structures mainly focus on the demountable steel-concrete composite beams and connections between components. For the demountable steel-concrete composite beams, the current solution is to replace the studs welded on the steel beam with bolts (Dai et al., 2015; Rehman et al., 2016). And for the component connections, the demountable function is achieved by setting the steel plate connection. For example, Senturk et al. (2020) and Pul et al. (2021) developed a novel monolithic-like precast beam-column and column-foundation connections for reinforced concrete (RC) structures. And the seismic performance of the proposed connections was determined by experimental investigation.

The wall is one of the critical components in the structure, which needs large building materials and working hours. If the demountable feature of the wall is realized, the environmental impact of buildings will be reduced significantly. However, there is a lack of research on demountable wall panels. The light-gauge steel framed (LSF) wall has been widely studied due to its superior characteristics, which is constructed by steel members and has great potential to realize the demountable function. The LSF is composed of light-gauge steel frame, interior and exterior wallboards, and insulation material (Telue & Mahendran, 2004). The light-gauge steel frame is mainly fabricated by C-shaped cold-formed steel (CFS). The wallboard can be plasterboard, steel sheet, cement fibrolite plate, or oriented strand board (OSB) (Javaheri-Tafti et al., 2014; Baran &

*Corresponding author. E-mail: *liucong@usts.edu.cn*

Alica, 2012; Zeynalian & Ronagh, 2015). LSF walls offer advantages over other technologies such as better aesthetics, lightweight, high strength-to-weight ratio, fast to construct, environmentally green, etc. (Sonkar et al., 2021; Mortazavi et al., 2018). Generally, the components of the CFS wall are connected by self-drilling screws, which are convenient to process (Casafont et al., 2006). But the connection of self-drilling screws makes disassembly very troublesome. Accordingly, the bolt connection with adjustable construction is designed in this paper to achieve the dismountability of the wall.

The mechanical behavior of the CFS wall is mainly influenced by the CFS frame. When this wall is applied in low-rise light structure residences, the LSF walls are usually used as a load-carrying member to withstand gravity loading and seismic action (Badr et al., 2019; Xu et al., 2021). The moment-resisting performance of the CFS frame was concerned (Mojtabaei et al., 2018, 2020, 2021; Ye et al., 2020). Papargyriou et al. (2021), Papargyriou and Hajirasouliha (2021) developed a practical design methodology for the seismic design of CFS strap-braced stud wall frames. The lateral load-resisting capacity, deformation capacity, ductility, and energy dissipation under lateral loading were investigated. For the medium and high-rise steel structure buildings, the wallboards are mainly used as nonbearing walls and withstand wind load (Selvaraj & Madhavan, 2019; Qiao et al., 2020). Selvaraj and Madhavan (2019) tested twenty sheathed CFS wall studs to investigate the structural effect of the sheathing under out-of-plane loading. The experimental results indicated that the CFS studs with vulnerability to fail in local buckling and lateral-torsional buckling could be braced effectively by the sheathing. In addition, the thermal characteristics of steel and insulation material are quite different. A thermal bridge is the main disadvantage of the LSF wall, resulting in problems of condensation and high energy loss in buildings (Wang & Salhab, 2009; Ariyanayagam et al., 2017). Traditionally the thermal bridge of the wall can be reduced by cutting slots with holes on the webs of CFS studs, which can increase the path of heat transfer. But the cost of this method is higher, and the bearing capacity of the CFS stud is reduced. In this paper, the composite wallboard sandwich method is adopted to enhance the insulation performance of the wall.

The investigation of the demountable behavior of the structure should include three aspects: the demountable implementation method, the demountable function verification, and the demountable advantage embodiment. There have been many demountable implementation methods, such as setting steel plate connections. However, the study of the demountable function verification is seldom. In addition, the advantages of demountable structure in environmental impact can be described by the life cycle assessment (LCA) method (Silvestre et al., 2015). This paper presents a demountable and modular light-gauge steel framed wall composed of CFS studs, timber frame, OSBs, and insulation material. The bolt replaces the screw to achieve the demountable function. The bending tests of five LSF wallboards were conducted to investigate the flexural behavior of the wallboard. The numerical model and the simplified calculation method of the flexural capacity of the wall were established. The demountable behavior of this wallboard was investigated by the secondary loading test and LCA method.

1. Details of DMLSF wallboard

The wallboard should meet the following requirements to achieve DfD:

(1) The wall can be dismantled conveniently, and once part of the wall is damaged, this part can be replaced rapidly, which can be realized by the bolt connection between the wall and mainframe. Moreover, the wall should be modular to enhance adaptability and convenience.
(2) The connection between the wall and the main frame should be adjustable to solve the error caused by repeated disassembly and assembly.
(3) The wall should possess enough insulation properties to meet the requirements of the different environments (e.g., cold regions) and building types.

The DMLSF wallboard in this paper has the following features to meet the above requirements: (1) All the components are connected by bolts, which can be dismantled conveniently. (2) The angle steels with slotted holes are used as the joint between the wall and beam, achieving a three-way adjustment function. (3) Insulation skeleton is set to weaken the thermal bridge of the wall (Liu et al., 2022).

The details of the DMLSF wallboard are shown in Figure 1. The CFS stud, fabricated by galvanized steel of Q235B grade, was used as the main load-bearing component. The middle part of the wallboard was an insulation skeleton made of timber with a lower thermal conductivity than steel, which was connected by bolts to the inner and outer steel frames. The interior of the wallboard was filled with high-efficiency thermal insulation material, referring to Expanded Polystyrene (EPS). The OSB with a thickness of 12 mm was adopted as the board of the DMLSF wall.

The beam and wallboard are connected by angle steel at the corner of each wallboard. The specifications of the two angle steels (Figure 1) are 50×6×100 mm and 50×6×40 mm. Each angle steel is connected with the CFS stud of the wallboard through a steel sleeve and an extension bolt. Error control capability is essential to demountable structures, which significantly affects the reuse time of the members. Therefore, slotted holes are set on the angle steels to achieve error adjustment. The connection of the two angle steels can realize the three-way adjustment function. All members, including the interior steel frame, insulation frame, and exterior steel frame, are connected by bolts. The distance between the bolts is 310 mm and 290 mm in vertical and horizontal directions, as shown in Figure 2.

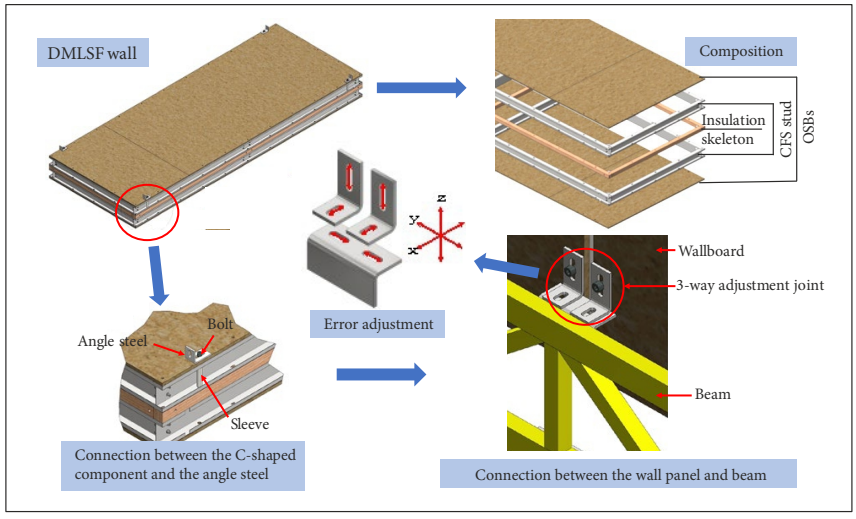

Figure 1. Composition of the DMLSF wallboard

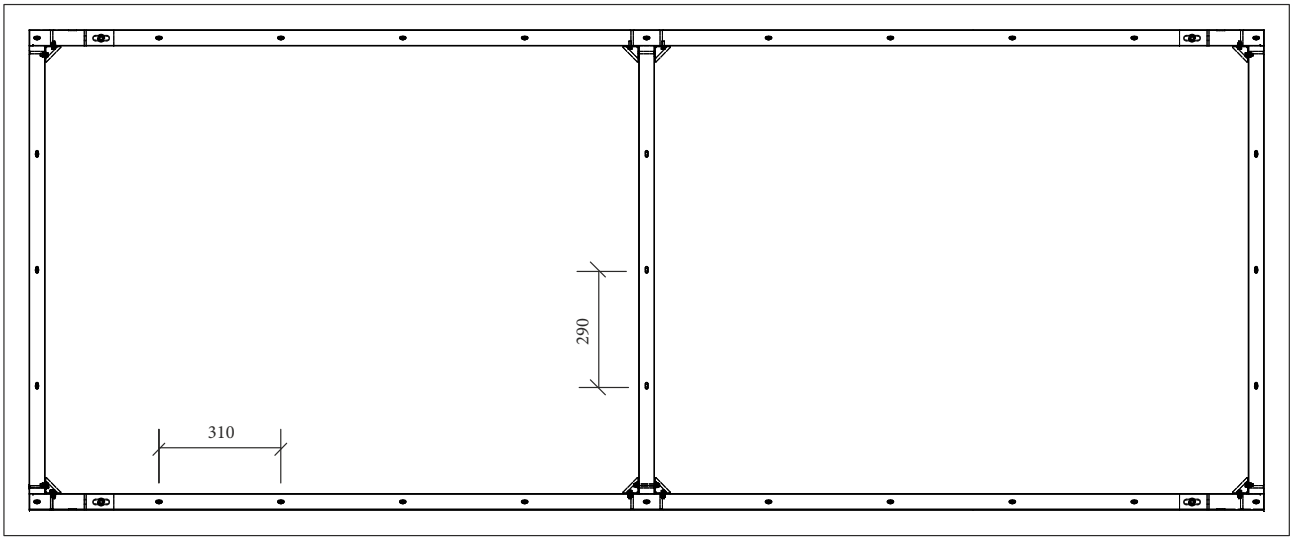

Figure 2. The bolt arrangement of the load-bearing frame (unit: mm)

The traditional splicing processing method for exterior wallboards is mostly sealant filling, which will reduce the construction speed and make the wallboard difficult to disassemble. The U-shaped side bubble sealing tapes used in the automotive industry are selected, as exhibited in Figure 3. The U-shaped card slot with a steel strip is clamped into the C-shaped steel curling edge, and the connection is substantial due to the presence of the steel strip. When the two wallboards are spliced, the side bubble is squeezed to achieve the sealing effect. Moreover, the inner and outer parts of the wallboard are equipped with sealing strips to enhance the sealing efficiency.

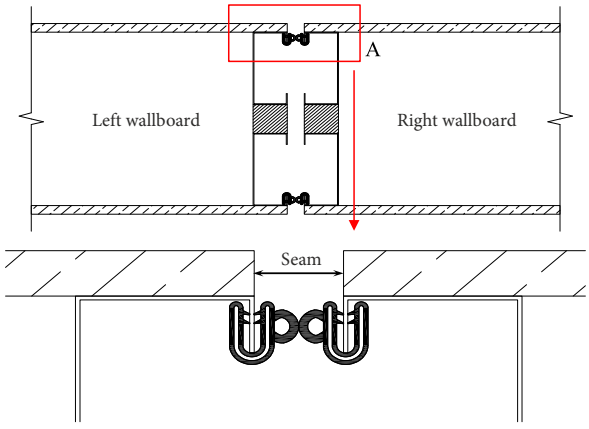

Figure 3. The seam of the DMLSF wallboard

2. Flexural behavior of the DMLSF wall

The flexural behavior of the DMLSF wall was investigated by experimental and numerical methods. The simplified calculation method was explored to realize the quick prediction of the bending capacity of this wallboard. Meanwhile, the sealing property test of the DMLSF wallboard seam has also been done to ensure that the seam remains sealed under the serviceability limit state.

2.1. Tests on flexural behavior of DMLSF wall module

The material properties of CFS were determined by three tensile coupon tests. The tests were conducted on an electronic universal material testing machine in accordance with GB/T 228.1 (Standards Press of China, 2010b). The average values of the members' yield strength and ultimate tensile strength measured in the tests were 257.55 MPa and 333 MPa, respectively.

Five specimens with different geometric parameters were designed to investigate the flexural performance of DMLSF wall modules. The height and width of all specimens were 3140 mm and 1200 mm, respectively. Figure 4 exhibits the definition and numbering rules of parameters in the specimen. The flange width and curl width of all CFS were 40 mm and 15 mm, respectively. The parameters of all specimens are listed in Table 1.

The test wallboard module was connected with the truss beam and placed on short concrete supports, as shown in Figure 5. The cross-section size of the column support was 500×300 mm. The truss height was 300 mm, and the cross-section size of the truss member was 50×50×4 mm. The uniform loading on the external surface of the wallboard was suitable for simulating realistic working conditions since the exterior walls were mainly subjected to wind loads. The weight loading was adopted in this paper. Three types of clump weights were used with the dimension of 300×150×40 mm (20 kg), 300×150×20 mm (10 kg), and 120×60×30 mm (2.5 kg), respectively. The clump weight of 20 kg was chosen in the initial stage of the test. When the wallboard reached the serviceability limit state, 10 kg clump weight was used. As the wallboard was further loaded near the ultimate limit state, the clump weight changed to 2.5 kg. The spacing of clump weights was set as 20 mm to avoid the arching effect. The clump weights were placed in stages, and the load was held for 2 min at each stage. In order to avoid accidents, the loading was terminated when the large visible plastic deformation of the wallboard occurred. Five displacement sensors were arranged, as shown in Figure 5. Strain gauges were attached to the CFS stud to monitor the strain during the loading process. Fourteen strain gauges were arranged at 100 mm away from the mid-span of the wallboard.

The load exerted by the weight was transformed into the uniform load. All specimens exhibited similar failure processes. The wallboard was always in elastic working condition at the initial loading stage. There was no significant deformation occurred at the adjustable joint between the wallboard and beam. The OSB had a certain degree of concave with the load increased because of the low stiffness.

Table 1. Specimen number and parameters

Number	H (mm)	H_1 (mm)	H_2 (mm)
90–60	264	90	60
100–40	264	100	40
100–60	284	100	60
110–40	284	110	40
110–60	304	110	60

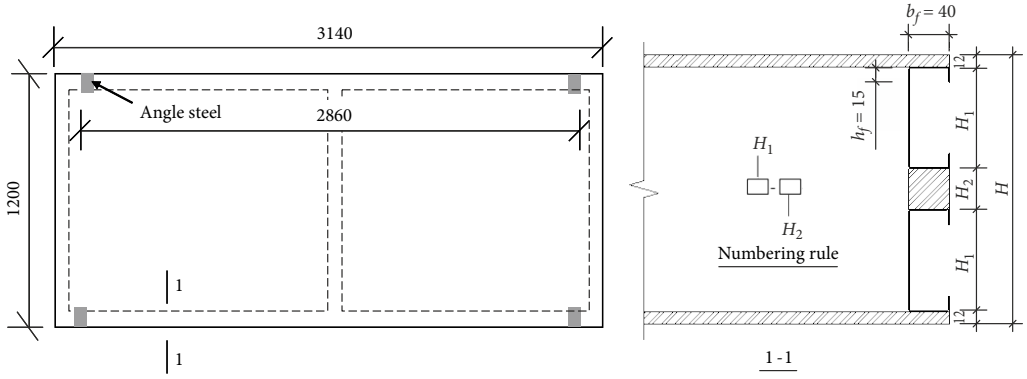

Figure 4. Definition and numbering rules of specimen parameters (unit: mm)

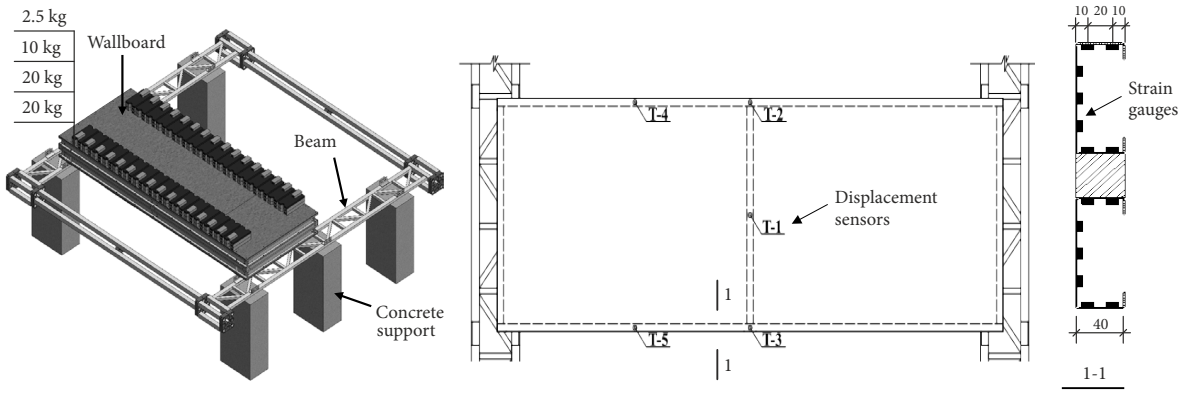

Figure 5. Test setup for bending performance (unit: mm)

When the load increased continuously, the wallboard showed noticeable deflection. As shown in Figure 6a, local buckling occurred at many locations of the flange, and the upper C-shaped cold-formed steel curled (Liu et al., 2022). A large gap gradually appeared between the OSB and the C-shaped steel upper flange, and the local buckling developed gradually towards the web of the upper CFS stud. In comparison, the local deformation of the lower CFS stud was not noticeable.

With the further increase of load, the local buckling of the web continued to develop. When the local buckling developed to the lower flange, the deflection of the wallboard increased sharply, and the wallboard reached the ultimate limit state. Meanwhile, the local buckling of the lower CFS stud also occurred in the same section, as presented in Figure 6b. The local buckling was influenced by the bolt that connected the LSF and OSB for the failure section. This bolt promoted the cooperation between CFS and OSB while increasing the local deformation. The deformation of the insulation skeleton was small throughout the test.

Figure 7a shows the load-displacement curves of the 100–40 wallboard obtained from the test. When the load increased from 0 to 1 kPa, all the components had no relative movement, and the deflection of the wallboard was slight. As the load increased, the load was mainly borne by CFS stud, which always maintained the elastic working state before the load reached 5 kPa. The local buckling of the CFS stud occurred when the load exceeded 5 kPa. When the last load level was exerted, the middle part of the CFS stud was in the plastic state, and the deflection increased suddenly. The maximum deflection is about 50 mm, which indicates the wallboard had superior ductility. The wallboard was a flexural member. When the load was exerted, the maximum displacement occurred at mid-span. Moreover, the wallboard bent in the direction of length and width. Therefore, in the initial loading stage, the vertical displacement of the wallboard under the same load level showed T1 > T3 > T5.

The deformation values at T1 of all specimens were obtained, and the corresponding load-displacement curves are illustrated in Figure 7b. The initial stage of load-displacement curves is almost linear for all specimens. When almost 85% of the ultimate strength was exceeded, the displacement began to increase significantly. The ultimate bearing capacity p of specimens 90–60, 100–40, 100–60, 110–40, and 110–60 are 5.63 kPa, 5.79 kPa, 6.48 kPa, 6.58 kPa and 6.69 kPa, respectively. The specimens with the same height have similar ultimate strengths, and the section of the CFS stud also influenced the ultimate strength of the specimen. The initial stiffness of the wallboard was mainly affected by the total section height and the joint connection performance between different components. The specimen 110–60 with the maximum total section height exhibited the maximum initial stiffness.

The load-strain curves are obtained by the monitoring data of strain gauges. The load-strain curves of specimen 110-60 are shown in Figure 8. The strain of the flange of CFS stud is the mean value of the two strain gauges. As the load increased from 0 to 6 kPa, each CFS stud was close to

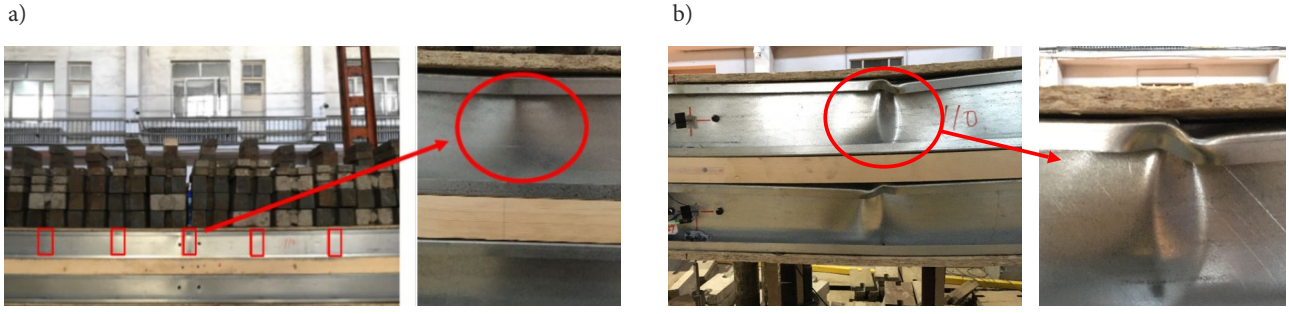

Figure 6. Deformation and failure mode of the wallboard during the test: a – Local buckling of CFS stud; b – Failure mode of the wallboard

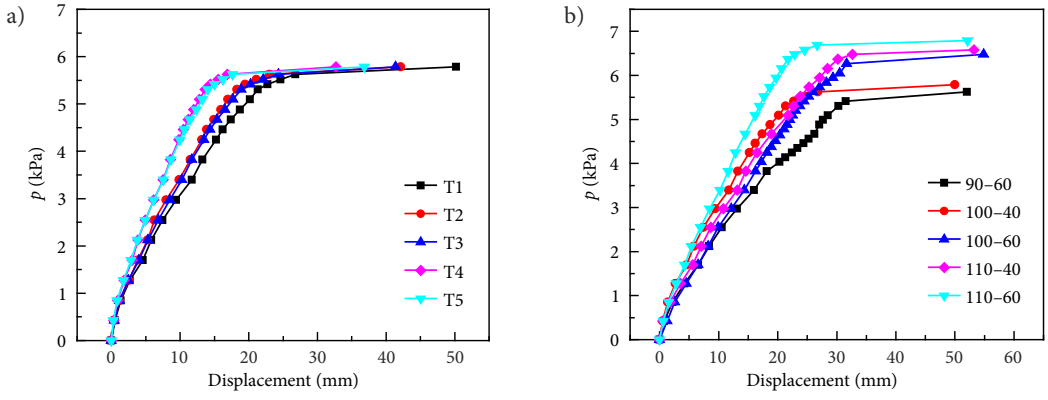

Figure 7. Load-displacement curves of specimens: a – Specimen 100–40; b – All specimens at midspan (T1)

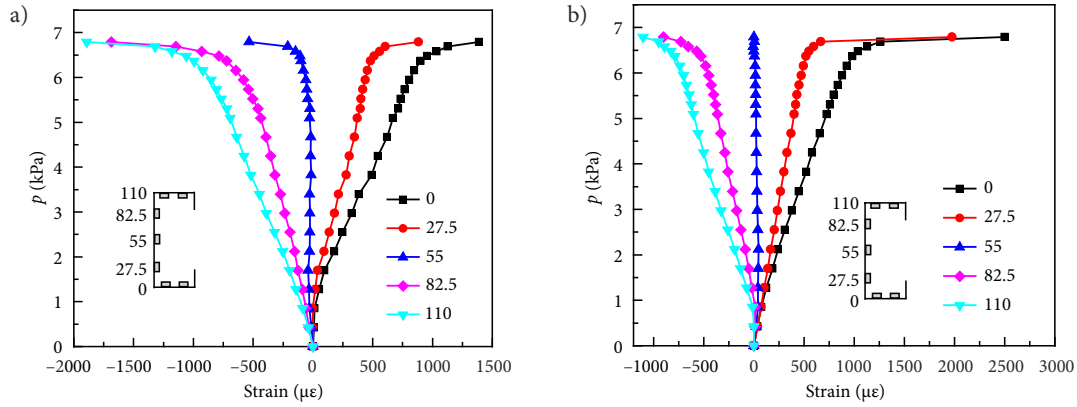

Figure 8. Load-strain curves of 110–60: a – Upper CFS stud; b – Lower CFS stud

working individually, mainly due to fewer bolts connecting the upper and lower CFS stud and weaker constraints on the elliptical bolt holes. When the load exceeded 6 kPa, local buckling occurred, and the restraining effect of bolts was enhanced. This deformation characteristic led to good energy dissipation performance of the wallboard.

According to the Chinese code "Technical standard for assembled buildings with steel-structure" (GB/T 51232-2016), the allowable deflection of lightweight exterior wallboards in the serviceability limit state is $\upsilon_Q = L/200$, where L is the span of the wallboard (Standards Press of China, 2016). In this paper, the allowable deflection of the wallboard is 14.3 mm. As illustrated in Figure 8b, all specimens are in elastic working state when the deflection is 14.3 mm. And the corresponding loads are between 3.5 kPa and 4.5 kPa, which demonstrates the wallboard proposed in this study meets the requirements of the Chinese code "Code of Structural Design Loads for Buildings" GB 50009-2012 for most multistory and high-rise buildings (Standards Press of China, 2012).

2.2. Numerical model and simplified calculation method of DMLSF wall

The software ANSYS Workbench was employed to develop the finite element model (FEM) of the DMLSF wall. The multilinear material model was selected to simulate the C-shaped steel. According to the tensile coupon tests, the yield strength and ultimate tensile strength of the C-shaped steel were set as 257.55 MPa and 333 MPa, and the corresponding strains were 0.0018 and 0.1. The initial elastic module was 1.43×10^5 MPa. The high-strength bolts with grade 8.8 were used, and the linear elastic material model was employed. The corresponding elastic modulus was 2.0×10^5 MPa, and the Poisson's ratio was 0.3. OSB panels were anisotropic materials with different material properties in parallel and vertical directions. The material model of OSB was set as "Orthotropic". According to the Chinese code "Oriented strand board", the elastic modulus in the parallel and vertical directions were 3500 MPa and 1400 MPa, and the Poisson's ratios were 0.31 and 0.12, respectively according to LY/T 1580-2010 (Standards Press of China, 2010a). The insulation frame was fabricated by pine timber, which was mainly bent along the grain during the test. Therefore, the anisotropy of timber was not considered, and the elastic modulus and Poisson's ratio were defined as 9400 MPa and 0.37.

The element type of the C-shaped steel and OSB was SHELL81, and the element SOLID185 was adopted to simulate the angle steel and insulation frame. Bolts were simulated by the beam element Beam188. The mesh sizes of the C-shaped steel and OSB were set as 20 mm and 40 mm. The mesh size of the insulation frame was the same as C-shaped steel. For the joint between the board and the beam, including the bolts, the sleeve and angle steel, the mesh sizes were all set as 3 mm. Figure 9a shows the FEM of the wallboard module. The boundary condition of the FEM is illustrated in Figure 9b. According to the bending test, the beam connected with the wallboard was ignored because of the weak influence on the result. Then, the surfaces of angle steels attached to the beam were set as rigid. The area of the uniform surface load is shown in Figure 9a and is the same as the location of the counterweight blocks in the test.

The numerical model of the DMLSF wallboard contained two settings for contact properties, namely "Frictionless" and "Bonded". "Frictionless" represents that the two contact surfaces are slippable tangentially and separable normally. "Bonded" indicates that no relative displacement is allowed in the normal and tangential directions of the two contact surfaces. During the test, a slight slip occurred between the C-shaped steel frame, OSB panel and insulation frame, and the influence of the friction force on the overall bending of the wallboard could be negligible, so the contact property between the C-shaped steel frame, OSB panel, and insulation frame was set as "Frictionless". In addition, the contact property between the bolt and the interfaces was set as "Bonded" to simplify the model. As is known to all, the stability of steel members can be easily affected by initial geometric imperfections, especially CFS members, whose section thickness is thinner (Ma et al., 2015; Qadir et al., 2020). In this paper, the CFS stud was reliably connected with OSB panel and insulation frame, and did not directly bear the concentrated load. Through the test, it was found that the bearing capacity of the wallboard was greatly affected by the connecting nodes. There-

fore, the influence of initial geometric imperfections on the stability of the wallboard was not considered in the model.

Figure 10 shows the comparison of failure modes of the specimen 110–40 obtained by test and FEM simulation. Both results show local buckling of the C-shaped steel at the sections with the bolts, which indicates the result obtained by FEM simulation agrees well with the test result. The comparison of the load-axial displacement curves between the FEM and corresponding tests is shown in Figure 11. The initial rising stage of the test curves is steeper than the FEM results. The reason is mainly that the preloads of bolts are ignored in FEM. In addition, the deformations of the numerical models when loaded to the final load are less than the experimental values. This phenomenon is mainly induced by the setting of the contact property of the bolt, which is stronger than the actual working condition of the bolt.

The flexural capacity of the wall is mainly affected by the section of the CFS stud. In addition, the constraints of bolts enhanced the combined effect of the two CFS studs, which resulted in a larger capacity of the wall with the higher height (H) and the same CFS stud. In order to obtain the simplified calculation method of the flexural capacity of the wall, 68 models were created and analyzed to explore the influence of the height of two CFS studs and insulation frame on the flexural capacity of the wall. As shown in Figure 12, with the same height of the insulation

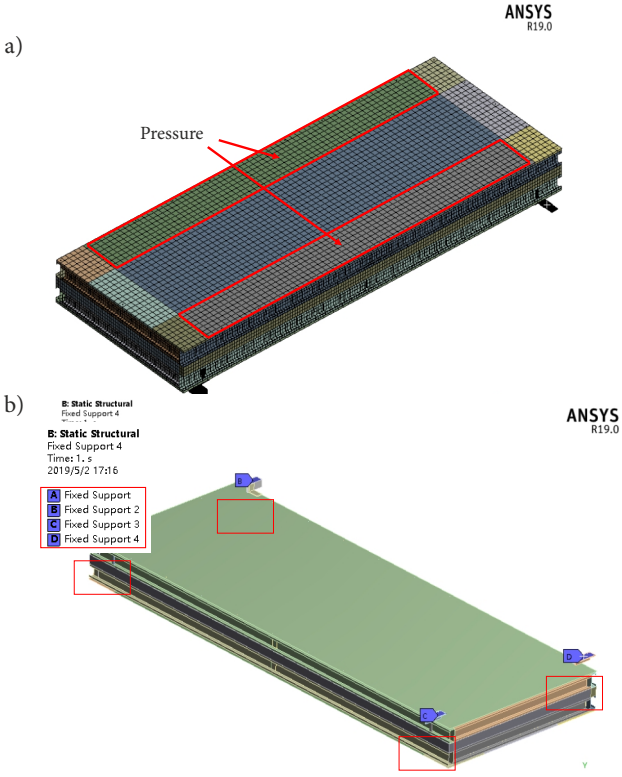

Figure 9. FEM and boundary condition of the DMLSF wallboard: a – FEM; b – Boundary condition of the model

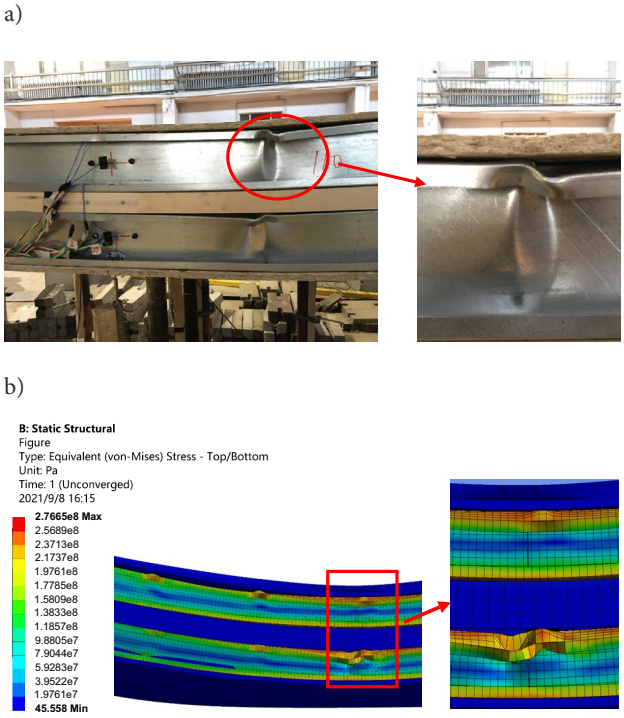

Figure 10. Comparison of failure mode obtained from test and FEM simulation: a – Failure mode obtained from test; b – Failure mode obtained from FEM simulation

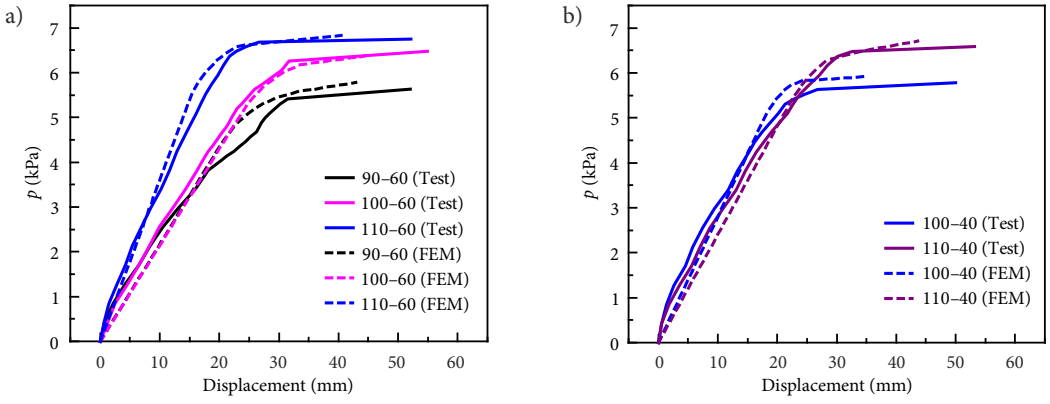

Figure 11. Comparison of load-displacement curves obtained from tests and FEM: a – 90–60, 100–60 and 110–60; b – 100–40 and 110–40

frame, the flexural capacity of the wall increases with the increase of the height of the CFS stud, while the increasing trend decreases gradually. When the height of the CFS stud is constant, the flexural capacity of the wall increases with the increase of the height of the insulation frame.

The bending moment borne by the section (Figure 4) can be calculated from the uniform load on the plate. Ignoring the influence of OSB plate, the calculation method of the flexural capacity of the wall panel can be obtained by fitting the data of numerical models as follows:

$$M = \frac{I_{eq} f_y}{H_1 + H_2/2}; \quad (1)$$

$$I_{eq} = 185.61 + 5.394 I_{e1} + 0.603 I_2 \text{ (unit: cm)}, \quad (2)$$

where M is the flexural strength of the section; f_y is the yield strength of CFS, which is equal to 257.55 MPa in this paper; I_{eq} is the equivalent section moment of inertia; I_{e1} is the effective net section moment of inertia for single CFS; I_2 is the section moment of inertia for the insulation frame. The R-squared of the fitting is 0.990, which means the calculated results of formulas (1) and (2) are very close to those of the numerical models, as shown in Figure 13.

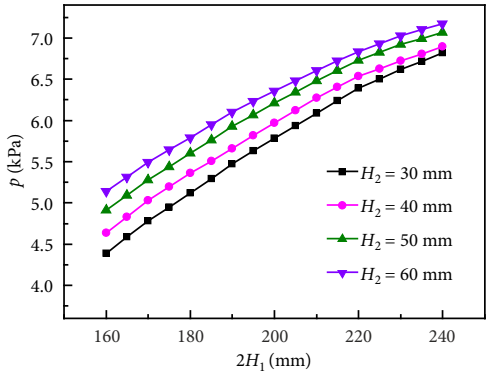

Figure 12. Relationship between the flexural capacity of the wall and section height of CFS stud and insulation frame

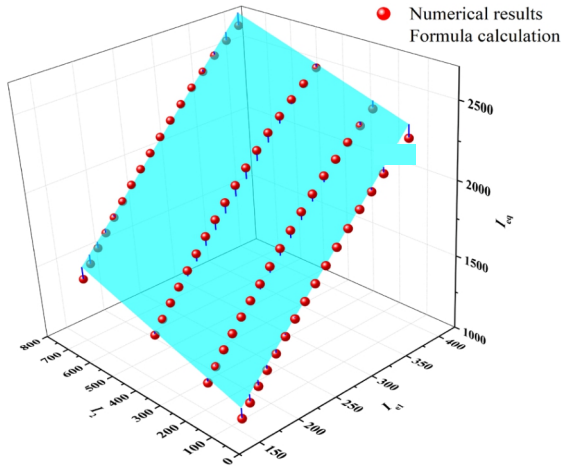

Figure 13. Equivalent section moment of inertia obtained by numerical modes and simplified formula

2.3. Reliability test of the seam of DMLSF wall

The seam of DMLSF wallboard is connected by the U-shaped side bubble sealing tapes, which are assembled by the curling of the CFS stud. The sealing strip is squeezed tightly by adjusting the gap between the wallboards to improve the airtightness of the outer cover structure. The reliability test of the seam was carried out to explore whether the gap would occur in the serviceability limit state. The wallboard 110–0 was selected for this test. The loading principle was multi-point loading on both sides of the wallboard (Figure 14). Two displacement sensors were arranged in the middle of the wallboard. The loading mode was also weight loading, and the loading stopped when the deflection reached $\upsilon_Q \pm 1$ mm. During the loading process, attention was paid to whether the extruded sealant strip at the joint had any visible gap, so the interior of the wallboard seam was not filled with insulation materials.

There was no separation of the sealing strip during the whole loading process (Figure 15). The load-displacement curves of the reliability test of the seam are shown in Figure 16. The weight load is transformed into the equivalent uniform load, and the equivalent area is half of each wall-

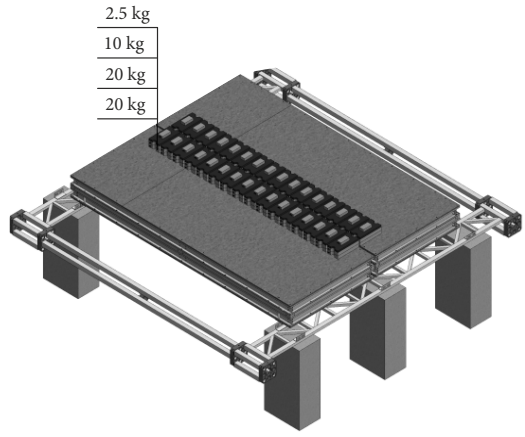

Figure 14. Test setup of the wallboard seam

Figure 15. Reliability test of the seam

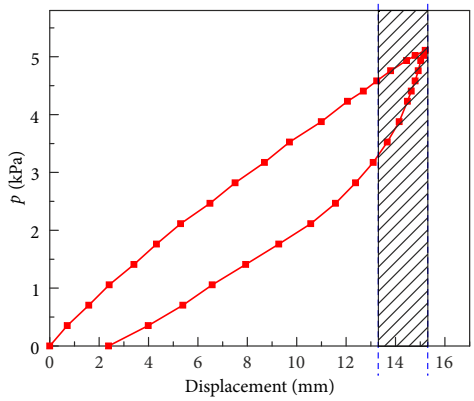

Figure 16. Load-displacement curves of the reliability test of the seam

board. The wallboard was always in elastic working state in the loading and unloading stage. When the deflection of the wallboard reaches the allowable value (15.2 mm), the load is about 5 kPa, which is consistent with the case of the secondary loading test. The reliability test results of the seam indicate that the seam of the DMLSF wallboard proposed in this study exhibits superior airtightness.

3. Demountable behavior of DMLSF wallboard

The advantage of the demountable structure is that components can be reused after disassembly. The demountable feature requires the component will not be subject to excessive irrecoverable deformation in the serviceability limit state. In addition, the LCA of the DMLSF wallboard was conducted to quantify environmental impacts, reflect the advantages of demountable behavior, and optimize wallboard construction from the perspective of environmental impact.

3.1. Secondary loading test of DMLSF wall

In this section, two DMLSF wallboards numbered 100-40 and 110–60 were tested. At first, the specimen was loaded until the deflection reached the allowable value. Then, the wallboard was disassembled entirely into small parts that were assembled again to verify the demountable feature of the wallboard. Finally, the bending test was carried out on the reassembled wallboard. For the first loading, when the deflection of the wallboard increased from 0 to $\upsilon_Q/3$, 20 kg clump weight was selected. Then the load continued to be applied by 10 kg clump weight until the deflection of the wallboard increased to $2\upsilon_Q/3$, and the 2.5 kg clump weight was used when the deflection of the wallboard increased from $2\upsilon_Q/3$ to υ_Q. The loading principle of secondary loading is the same as that of Section 3.1.

The loading method is weight loading, making it difficult to load to the deflection of υ_Q accurately. Therefore, the loading stopped when the deflection reached $\upsilon_Q \pm 1$ mm. The wallboard bends significantly, while no local buckling of LSF was observed when the deflection reached υ_Q. After unloading, the wallboard was completely disassembled into different components and reassembled again for the secondary loading. The deformation and failure modes were the same as those in Section 3.1. The ultimate bearing capacity p and initial stiffness k for the secondary loading test are listed in Table 2. The ultimate bearing capacity of specimens 100–40 and 110–60 in the initial loading is about 75% of that in the secondary loading test. In comparison, the initial stiffness of the initial loading is basically the same as that of the secondary loading test.

Figure 17 shows the load-displacement curves of the 100–40 and 110–60 wallboard in the secondary loading test. During the loading process, the curves of the initial loading are consistent with that of secondary loading. At the beginning of unloading, the recovery value of displacement was small. As the unloading value increases, the recovery value of displacement gradually increases. When the load is completely removed, the displacement recovers to about 3 mm. The reason for the above test results is that

Table 2. The ultimate strength and initial stiffness for the secondary loading test

Specimens	Loading	p (kPa)	k ($\times 10^{-3}$N/mm^3)
100–40	Initial loading	4.25	0.25
	Secondary loading	5.79	0.27
110–60	Initial loading	5.21	0.33
	Secondary loading	6.79	0.33

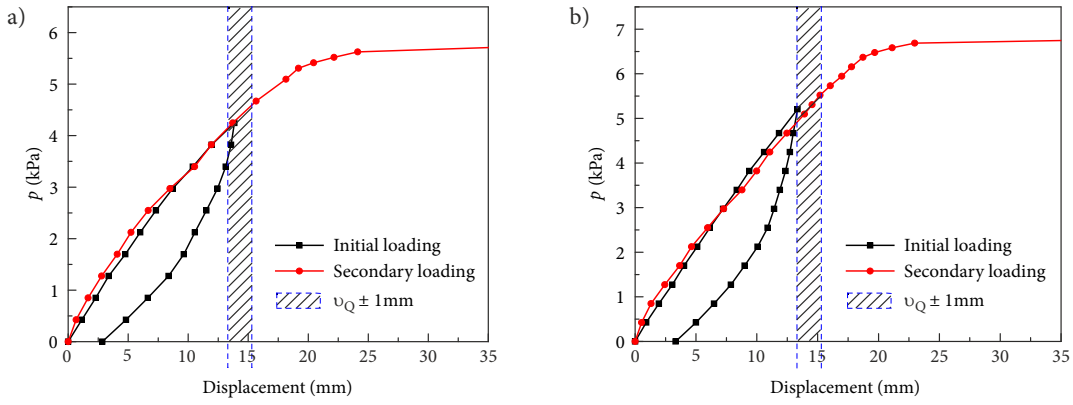

Figure 17. Load-displacement curves for secondary loading test: a – 100–40; b – 110–60

the elliptical holes of the bolts can cause inevitable sliding and friction between the different components of the wallboard during the loading process, which also makes the wallboard possess the energy consumption capacity without plastic deformation.

3.2. Life cycle assessment of the wallboard

The construction industry contributes significantly to the global consumption of raw materials and energy (Cabeza et al., 2014). The environmental impact of the building is dominated by the consumption of resources and the generation of waste. Thus, the demountable structures possess the apparent advantage of reusing components, which can significantly reduce the negative environmental impact of building structures. Currently, LCA methods are frequently applied to evaluate the environmental properties of buildings and building elements and incorporated into the construction decisions, such as the selection of environmentally friendly materials and products (Butt et al., 2016; Evangelista et al., 2018). In general, non-renewable energy consumption (PE-NRe) and potential global warming (GWP) are the most influential factors on the environmental impacts of buildings (Kurda et al., 2020). The PE-NRe is used to measure the non-renewable energy consumed in the model's life cycle. GWP refers to the amount of carbon dioxide and other harmful gases produced by burning fossil fuels.

The Simapro 9.0 software was adopted, and the methods of IPCC2013 and Cumulative Energy Demand (CED) were used to analyze the GWP and PE-NRe, respectively. The Ecoinvent database was adopted, containing life cycle inventory (LCI) data from various sectors, such as energy production, transport, building materials, production of chemicals, metal production, and fruit and vegetables. The entire database consists of over 10,000 interlinked datasets, each describing a life-cycle inventory at the process level.

3.2.1. Case collection

Four cases were adopted to conduct comparative studies in this paper. The influence of the number of reuse times and the renewal of part components of the DMLSF wallboard on environmental impact was discussed. In addition, a comparative analysis between the DMLSF wallboard and the autoclaved aerated concrete block wall was also performed. All transportation distance is assumed to be 20 km, and the processing is represented by power consumption.

(1) Case 1: the DMLSF wallboard module

The first case is the DMLSF wallboard, and the function unit is one module with the size of 3140×1200×264 mm (100–40). Each part of the module can be assembled by hand. The lifetime of the module is assumed to be 50 years. The quantities of materials per unit are shown in Table 3. The stage of raw material procurement, manufacturing, transportation, installation, and waste management are considered. The system boundary is defined (Figure 18a). The cold-formed C-shaped steel is formed by bending steel plate. The bolts are purchased directly from stores, as are OSB, wood and EPS. The environmental impact of these materials can be considered directly through the built-in material library of the software Simapro. The extrusion, cutting, drilling, and other operation are carried out on materials according to the specifications when the materials are transported to the fabrication plant. Then, all the components are assembled into one module, which is delivered to the construction site and installed. Finally, the module is demolished and disposed of as waste when the building reaches its service life.

(2) Case 2: Secondary reuse of the module of DMLSF wallboard

Many buildings are demolished when they are far from 50 years old, usually for reasons other than material degradation. It is assumed that this module has been used for the first time for 25 years and then disassembled,

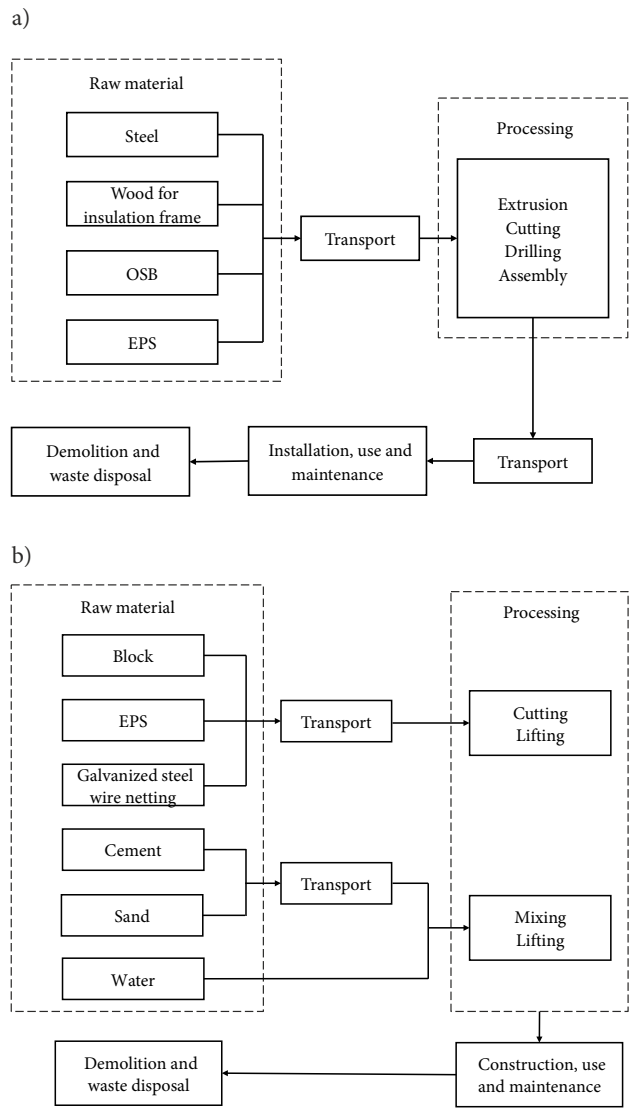

Figure 18. System boundaries of cases

transported to another location, and reused for another 25 years. Compared with the first case, the process of disassembly and transportation increased, but the consumption of materials and manufacturing was reduced.

(3) Case 3: the module of DMLSF wallboard with partial replacement

The third case is similar to the second case. The two OSBs are assumed to be damaged when the module is disassembled. Then, the module is repaired by replacing the damaged OSBs. The repaired module is transported and reused for another building.

(4) Case 4: the autoclaved aerated concrete block (AACB) wall

The fourth case is the AACB wall with the same area as the wall module. It contains autoclaved aerated concrete blocks of 600×200×200 mm, cement mortar, galvanized steel wire netting, and EPS with a thickness of 50 mm. The quantities of materials per unit are shown in Table 3, and the system boundary is defined as shown in Figure 18b. The blocks, EPS, galvanized steel wire netting, cement, and sand can be purchased directly, and the environmental impact can be considered through the built-in material library of the software. The mortar is composed of cement, sand, and water in the ratio of 1:3:0.65.

Table 3. Materials consumption of one module of DMLSF wallboard and AACB wall

Material		Quantity (kg)
DMLSF wallboard	Steel	45.09
	Wood	9.25
	OSB	58.79
	EPS	17.56
AACB wall	Block	403.2
	Cement mortar (cement: sand: water = 1:3:0.65)	160.0
	EPS	3.6
	Galvanized steel wire netting	3.21

3.2.2. Analysis and discussion

GWP represents the mass of carbon dioxide equivalent to the greenhouse effect of various greenhouse gases over a 100-year time frame, which is an essential indicator of environmental impact. The GWP of the first and the fourth cases are shown in Figure 19. The total GWP of the DMLSF wall module is 302 kg CO_2 eq, which is lower than that of the AACB wall with the same area (327 kg CO_2 eq). The result indicates that the environmental impact of the DMLSF wall is lower than that of the AACB wall. Further considering the environmental impact of each material of the DMLSF wall, steel and EPS contribute the most to the environmental impact. The sum of their GWP is about 57% of the total GWP. For AACB walls, blocks contribute 191 kg CO_2 eq, about 59% of the total GWP. Therefore, the consumption of steel and EPS should be reduced as much as possible to meet the performance requirements of DMLSF walls. In addition, the environmental impact of transport is relatively small. Then for the second case, the increased CO_2 emissions are minor because only the transport process is increased. Compared with making new wallboard, its environmental impact is significantly reduced. When the OSBs are damaged during the turnover process, as illustrated in Case 3, the CO_2 emissions of DMLSF wall module are recalculated. The GWP of Case 3 is 339 kg CO_2 eq, which can still substantially reduce the environmental impact compared with making a new one. Therefore, the demountable structure can significantly reduce the environmental impact of the construction structure through the reuse of modules, even if some internal components need to be replaced.

PE-NRe represents energy consumption. The categories including "Non-renewable, fossil", "Non-renewable, nuclear" and "Non-renewable, biomass" are considered. In order to obtain the total energy demand (PE-NRe), each impact category is given the weighting factor 1. The PE-NRe of the first and the fourth cases are shown in Figure 20. The PE-NRe of DMLSF wall (Case 1) module is 4004 MJ, which is higher than that of AACB wall (Case 4) with the same area (2775 MJ). For the DMLSF wall module, the energy consumption of EPS is the most prominent, accounting for 40% of the total energy consumption. And the block consumes the most energy for AACB wall, which is about 49% of the total energy consumption.

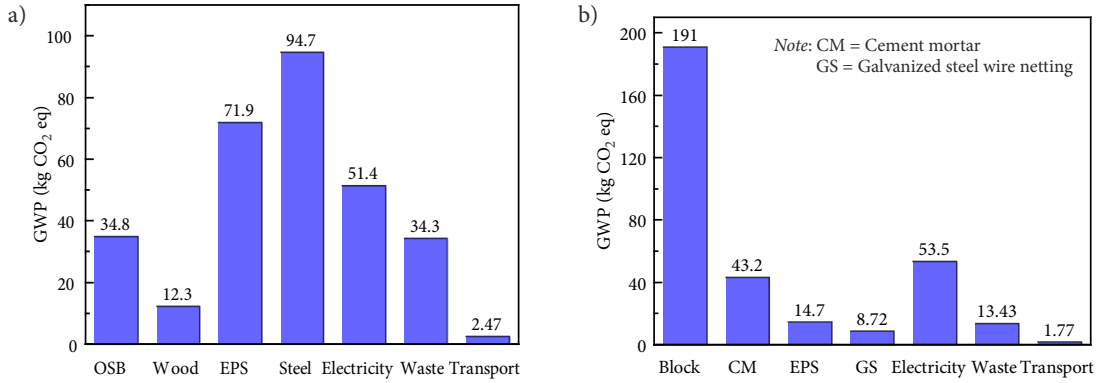

Figure 19. GWP of the DMLSF wall and AACB wall: a – DMLSF wall; b – AACB wall

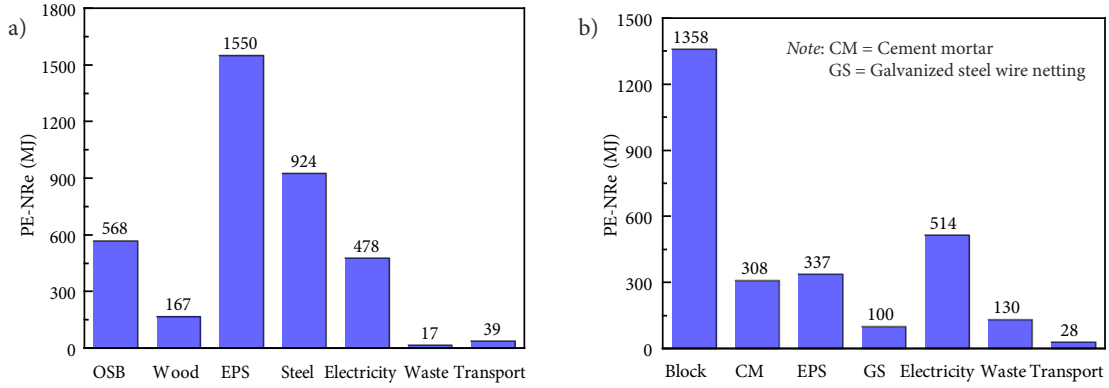

Figure 20. PE-NRe of the DMLSF wall and AACB wall: a – DMLSF wall; b – AACB wall

For the second case, the energy consumption of reuse mainly comes from transportation, which is relatively small. The PE-NRe of the third case is 4611 MJ, which is still less than twice the energy consumption of the AACB wall.

In summary, the environmental impact of the DMLSF wall is less than that of the AACB wall, and the energy consumption of the DMLSF wall is relatively more significant if the component is only used once. Once a component is reused, this can drastically reduce environmental impact and energy consumption, even if localized elements need to be replaced. For the composition of the DMLSF wall, the energy consumption and environmental impact of insulation materials are prominent. Therefore, seeking more environmentally friendly insulation materials is the key to reducing the environmental impact and energy consumption of the wall.

Conclusions

Many buildings are demolished before reaching their service life, which results in material waste and environmental pollution. This paper presents a demountable and modular LSF wall to realize the reuse of components. The flexural and demountable behavior of the wall is investigated by experimental, numerical, and LCA methods. According to the investigation, the following conclusions can be drawn:

(1) The DMLSF wall can be easily assembled and disassembled with bolts. For the bending tests, the wallboard was in elastic working condition at the initial loading stage, and then local buckling occurred in many positions of the flange and curling of the upper CFS stud. The wallboard reached the ultimate limit state when the local buckling of the lower CFS stud occurred.

(2) The tested wallboards were always in elastic working state before the load reached 5 kPa. The ultimate defection of all specimens was close to 50 mm. The interaction between the upper and lower CFS stud is weak when the load increases from 0 to 6 kPa because there are fewer bolted connections and the restraining effect of the elliptical bolt holes is weak. The numerical model was established and verified by test results. The simplified calculation method of the flexural capacity of the wall was proposed to realize the quick prediction.

(3) For the reliability test of the seam of the DMLSF wall, there was no separation of the sealing strip during the whole loading process, which indicated that the seam of the DMLSF wallboard proposed in this study exhibited superior airtightness.

(4) For the secondary loading test, the curve of the secondary loading is consistent with that of the initial loading. During the unloading phase, the displacement returned to about 3 mm when the load was removed entirely due to the elliptical holes of the bolts facilitating a certain sliding and friction of the different components during the loading process.

(5) The result of the life cycle assessment of the DMLSF wall effectively demonstrates the advantages of demountable structures. The environmental impact and energy consumption of the DMLSF wall mainly come from raw materials, especially insulation material. Once the module is reused, its environmental impact and energy consumption will be significantly reduced compared with making a new one.

Acknowledgements

This work was supported by the National Natural Science Foundation of China (No. 52208187 & 52178294), the Natural Science Foundation of Jiangsu Province (No. BK20200990), and the Science and Technology Program of Suzhou (No. SYG202113). This support is gratefully acknowledged.

Funding

This work was supported by the National Natural Science Foundation of China (No. 52208187 & 52178294), the Natural Science Foundation of Jiangsu Province (No. BK20200990), and the Science and Technology Program of Suzhou (No. SYG202113).

Author contributions

Cong LIU and Xin CHEN conceived the study and were responsible for the design and development of the data analysis. Xiaoyong MAO and Jian YUAN were responsible for data collection and analysis. Cong LIU and Lin HE were responsible for data interpretation. Cong LIU wrote the first draft of the article.

Disclosure statement

The authors declare that they do not have any competing financial, professional, or personal interests from other parties.

References

Ariyanayagam, A. D., Keerthan, P., & Mahendran, M. (2017). Thermal modelling of load bearing cold-formed steel frame walls under realistic design fire conditions. *Advanced Steel Construction*, *13*(2), 160–189. https://doi.org/10.18057/IJASC.2017.13.2.5

Badr, A. R., Elanwar, H. H., & Mourad, S. A. (2019). Numerical and experimental investigation on cold-formed walls sheathed by fiber cement board. *Journal of Constructional Steel Research*, *158*, 366–380. https://doi.org/10.1016/j.jcsr.2019.04.004

Baran, E., & Alica, C. (2012). Behavior of cold-formed steel wall panels under monotonic horizontal loading. *Journal of Constructional Steel Research*, *79*, 1–8. https://doi.org/10.1016/j.jcsr.2012.07.020

Butt, A. A., Birgisson, B., & Kringos, N. (2016). Considering the benefits of asphalt modification using a new technical life cycle assessment framework. *Journal of Civil Engineering and Management*, *22*(5), 597–607. https://doi.org/10.3846/13923730.2014.914084

Cabeza, L. F., Rincon, L., Vilarino, V., Perez, G., & Castell, A. (2014). Life cycle assessment (LCA) and life cycle energy analysis (LCEA) of buildings and the building sector: A review. *Renewable and Sustainable Energy Reviews*, *29*, 394–416. https://doi.org/10.1016/j.rser.2013.08.037

Casafont, M., Arnedo, A., Roure, F., & Rodríguez-Ferran, A. (2006). Experimental testing of joints for seismic design of lightweight structures. Part 1. Screwed joints in straps. *Thin-Walled Structures*, *44*(2), 197–210. https://doi.org/10.1016/j.tws.2006.01.002

Dai, X. H., Lam, D., & Saveri, E. (2015). Effect of concrete strength and stud collar size to shear capacity of demountable shear connectors. *Journal of Structural Engineering*, *141*(11), 04015025. https://doi.org/10.1061/(ASCE)ST.1943-541X.0001267

Eckelman, M. J., Brown, C., Troup, L. N., Wang, L., Webster, M. D., & Hajjar, J. F. (2018). Life cycle energy and environmental benefits of novel design-for-deconstruction structural systems in steel buildings. *Building and Environment*, *143*, 421–430. https://doi.org/10.1016/j.buildenv.2018.07.017

Evangelista, P., Kiperstok, A., Torres, E. A., & Goncalves, J. P. (2018). Environmental performance analysis of residential buildings in brazil using life cycle assessment (LCA). *Construction and Building Materials*, *169*, 748–761. https://doi.org/10.1016/j.conbuildmat.2018.02.045

Javaheri-Tafti, M. R., Ronagh, H. R., Behnamfar, F., & Memarzadeh, P. (2014). An experimental investigation on the seismic behavior of cold-formed steel walls sheathed by thin steel plates. *Thin-Walled Structures*, *80*, 66–79. https://doi.org/10.1016/j.tws.2014.02.018

Kurda, R., Brito, J. D., & Silvestre, J. D. (2020). A comparative study of the mechanical and life cycle assessment of high-content fly ash and recycled aggregates concrete. *Journal of Building Engineering*, *29*, 101173. https://doi.org/10.1016/j.jobe.2020.101173

Liu, C., Mao, X. Y., He, L., Chen, X., Yang, Y., & Yuan, J. (2022). A new demountable light-gauge steel framed wall: Flexural behavior, thermal performance and life cycle assessment. *Journal of Building Engineering*, *47*, 103856. https://doi.org/10.1016/j.jobe.2021.103856

Ma, W., Becque, J., Hajirasouliha, I., & Ye, J. (2015). Cross-sectional optimization of cold-formed steel channels to Eurocode 3. *Engineering Structures*, *101*, 641–651. https://doi.org/10.1016/j.engstruct.2015.07.051

Mojtabaei, S. M., Kabir, M. Z., Hajirasouliha, I., & Karhar, M. (2018). Analytical and experimental study on the seismic performance of cold-formed steel frames. *Journal of Constructional Steel Research*, *143*, 18–31. https://doi.org/10.1016/j.jcsr.2017.12.013

Mojtabaei, S. M., Becque, J., & Hajirasouliha, I. (2020). Local buckling in cold-formed steel moment-resisting bolted connections: Behavior, capacity, and design. *Journal of Structural Engineering*, *146*(9), 04020167. https://doi.org/10.1061/(ASCE)ST.1943-541X.0002730

Mojtabaei, S. M., Becque, J., & Hajirasouliha, I. (2021). Behavior and design of cold-formed steel bolted connections subjected to combined actions. *Journal of Structural Engineering*, *147*(4), 04021013. https://doi.org/10.1061/(ASCE)ST.1943-541X.0002966

Mortazavi, M., Sharafi, P., Ronagh, H., Samali, B., & Kildashti, K. (2018). Lateral behaviour of hybrid cold-formed and hot-rolled steel wall systems: Experimental investigation. *Journal of Constructional Steel Research*, *147*, 422–432. https://doi.org/10.1016/j.jcsr.2018.04.035

Papargyriou, I., & Hajirasouliha, I. (2021). More efficient design of CFS strap-braced frames under vertical and seismic loading. *Journal of Constructional Steel Research*, *185*, 106886. https://doi.org/10.1016/j.jcsr.2021.106886

Papargyriou, I., Hajirasouliha, I., Becque, J., & Pilakoutas, K. (2021). Performance-based assessment of CFS strap-braced stud walls under seismic loading. *Journal of Constructional Steel Research*, *183*, 106731. https://doi.org/10.1016/j.jcsr.2021.106731

Parastesh, H., Hajirasouliha, I., & Ramezani, R. (2014). A new ductile moment-resisting connection for precast concrete frames in seismic regions: An experimental investigation. *Engineering Structures*, *70*(9), 144–157. https://doi.org/10.1016/j.engstruct.2014.04.001

Pul, S., Senturk, M., Ilki, A., & Hajirasouliha, I. (2021). Experimental and numerical investigation of a proposed monolithic-like precast concrete column-foundation connection. *Engineering Structures*, *246*, 113090. https://doi.org/10.1016/j.engstruct.2021.113090

Qadir, S. J., Nguyen, V. B., Hajirasouliha, I., Cartwright, B., & English, M. A. (2020). Optimal design of cold roll formed steel channel sections under bending considering both geometry and cold work effects. *Thin-Walled Structures*, *157*, 107020. https://doi.org/10.1016/j.tws.2020.107020

Qiao, W., Yan, X., Zhu, R., Wang, F., & Wang, D. (2020). Flexural properties of new cold-formed thin-walled steel and concrete composite slabs. *Journal of Building Engineering*, *31*, 101441. https://doi.org/10.1016/j.jobe.2020.101441

Rehman, N., Lam, D., Dai, X., & Ashour, A. F. (2016). Experimental study on demountable shear connectors in composite slabs with profiled decking. *Journal of Constructional Steel Research*, *122*, 178–189. https://doi.org/10.1016/j.jcsr.2016.03.021

Selvaraj, S., & Madhavan, M. (2019). Flexural behaviour and design of cold-formed steel wall panels sheathed with particle cement board. *Journal of Constructional Steel Research*, *162*, 105723. https://doi.org/10.1016/j.jcsr.2019.105723

Senturk, M., Pul, S., Ilki, A., & Hajirasouliha, I. (2020). Development of a monolithic-like precast beam-column moment connection: Experimental and analytical investigation. *Engineering Structures*, *205*, 110057. https://doi.org/10.1016/j.engstruct.2019.110057

Silvestre, J. D., Silva, A., & Brito, J. D. (2015). Uncertainty modelling of service life and environmental performance to reduce risk in building design decisions. *Journal of Civil Engineering and Management*, *21*(3), 308–322. https://doi.org/10.3846/13923730.2014.890649

Sonkar, C., Bhattacharyya, S. K., & Mittal, A. K. (2021). Investigations on cold-formed steel wall panels with different sheathing boards under axial loading: Experimental and analytical/semi-analytical studies. *Journal of Building Engineering*, *44*, 102924. https://doi.org/10.1016/j.jobe.2021.102924

Standards Press of China. (2010a). *Oriented strand board* (LY/T 1580-2010). Beijing, China.

Standards Press of China. (2010b). *Metallic materials-Tensile testing – Part 1: Method of test at room temperature* (GB/T 228.1-2010). Beijing, China.

Standards Press of China. (2012). *Load code for the design of building structures* (GB 50009-2012). Beijing, China.

Standards Press of China. (2016). *Technical standard for assembled buildings with steel-structure* (GB/T 51232-2016). Beijing, China.

Telue, Y., & Mahendran, M. (2004). Behaviour and design of cold-formed steel wall frames lined with plasterboard on both sides. *Engineering Structures*, *26*(5), 567–579. https://doi.org/10.1016/j.engstruct.2003.12.003

Wang, Y. C., & Salhab, B. (2009). Structural behaviour and design of lightweight structural panels using perforated cold-formed thin-walled sections under compression. *International Journal of Steel Structures*, *9*, 57–67. https://doi.org/10.1007/BF03249480

Xiao, J., Ding, T., & Zhang, Q. (2017). Structural behavior of a new moment-resisting DfD concrete connection. *Engineering Structures*, *132*, 1–13. https://doi.org/10.1016/j.engstruct.2016.11.019

Xu, Y., Zhou, X., Shi, Y., Zou, Y., Xiang, Y., & Xu, L. (2021). Experimental investigation of shear resistance of cold-formed steel framed sheathed walls. *Journal of Constructional Steel Research*, *178*(3), 106488. https://doi.org/10.1016/j.jcsr.2020.106488

Ye, J., Mojtabaei, S.M., Hajirasouliha, I., & Pilakoutas, K. (2020). Efficient design of cold-formed steel bolted-moment connections for earthquake resistant frames. *Thin-Walled Structures*, *150*, 105926. https://doi.org/10.1016/j.tws.2018.12.015

Zeynalian, M., & Ronagh, H. R. (2015). Seismic performance of cold formed steel walls sheathed by fibre-cement board panels. *Journal of Constructional Steel Research*, *107*, 1–11. https://doi.org/10.1016/j.jcsr.2015.01.003